The Astrophysical Journal, 659:758–772, 2007 April 10

ON THE MAGNETIC FLUX BUDGET IN LOW-CORONA MAGNETIC RECONNECTION AND INTERPLANETARY CORONAL MASS EJECTIONS

Jiong Qiu,[1] Qiang Hu,[2] Timothy A. Howard,[1] and Vasyl B. Yurchyshyn[3]

Received 2006 September 11; accepted 2006 December 12

ABSTRACT

We present the first quantitative comparison between the total magnetic reconnection flux in the low corona in the wake of coronal mass ejections (CMEs) and the magnetic flux in magnetic clouds (MCs) that reach 1 AU 2–3 days after CME onset. The total reconnection flux is measured from flare ribbons, and the MC flux is computed using in situ observations at 1 AU, all ranging from 10^{20} to 10^{22} Mx. It is found that for the nine studied events in which the association between flares, CMEs, and MCs is identified, the MC flux is correlated with the total reconnection flux Φ_r. Further, the poloidal (azimuthal) MC flux Φ_p is comparable with the reconnection flux Φ_r, and the toroidal (axial) MC flux Φ_t is a fraction of Φ_r. Events associated with filament eruption do not exhibit a different $\Phi_{t,p}$-Φ_r relation from events not accompanied by erupting filaments. The relations revealed between these independently measured physical quantities suggest that for the studied samples, the magnetic flux and twist of interplanetary magnetic flux ropes, reflected by MCs, are highly relevant to low-corona magnetic reconnection during the eruption. We discuss the implications of this result for the formation mechanism of twisted magnetic flux ropes, namely, whether the helical structure of the magnetic flux rope is largely pre-existing or formed in situ by low-corona magnetic reconnection. We also measure magnetic flux encompassed in coronal dimming regions (Φ_d) and discuss its relation to the reconnection flux inferred from flare ribbons and MC flux.

Subject headings: solar-terrestrial relations — Sun: activity — Sun: coronal mass ejections (CMEs) — Sun: flares — Sun: magnetic fields

Online material: color figure

1. INTRODUCTION

Coronal mass ejections (CMEs) observed by satellites at 1 AU are called interplanetary coronal mass ejections (ICMEs). Another term, magnetic clouds (MCs), is also frequently used, sometimes interchangeably with ICMEs. An MC, however, is defined by a low-β structure with stronger magnetic fields and a lower ion (mostly proton) temperature than the ambient solar wind, which exhibits a smooth rotation of the magnetic field direction when measured by a spacecraft moving across it (Burgala et al. 1990; Lepping et al. 1990, 1997). It is believed that the unique magnetic flux rope structure of MCs originates from the Sun, and evidence has been found that parts of MCs at 1 AU are still anchored to the Sun's surface (e.g., Gosling 1990). Understanding the magnetic flux budget in terms of the in situ measurements of MCs in relation to the solar source has been an outstanding issue, closely related to the question of the mechanism creating magnetic flux ropes in the first place.

Observational effort has been made in the past decade to relate magnetic clouds to various solar progenitors (Bothmer & Schwenn 1994; Rust 1994; Marubashi 1997; Zhao & Hoeksema 1998; McAllister & Martin 2000; Yurchyshyn et al. 2001, 2005; Nindos et al. 2003; Ruzmaikin et al. 2003; Hu et al. 2005; Luoni et al. 2005; Rust et al. 2005; Krall et al. 2006). Lepping et al. (1997), Bothmer & Rust (1997), and Crooker (2000) associated solar filaments or prominences with MCs. However, there is abundant observational evidence suggesting that a good fraction of MCs, particularly those originating from solar active regions, are not preceded by erupting filaments (e.g., Subraminian & Dere 2001). Canfield et al. (1999) and Leamon et al. (2002) associated the soft X-ray sigmoid structures with CMEs. In a very few studies, quantitative comparisons have been given between properties of magnetic clouds, typically magnetic flux and helicity, and the solar progenitors, such as magnetic flux in filaments (Lepping et al. 1997), coronal dimming flux (Webb et al. 2000; Mandrini et al. 2005; Attrill et al. 2006), and the total magnetic flux and helicity in source active regions (Leamon et al. 2004).

Concerning the solar origin of interplanetary flux ropes, whereas some investigators take the global view (Crooker 2000; Mulligan et al. 2000), there are also numerous models for the formation of flux ropes locally. We categorize these "local" models into three pictures. In the first picture, magnetic flux ropes emerge from below the Sun's surface (Low 1994; Chen 1989; Fan & Gibson 2004). In the second picture, magnetic flux ropes are formed in the low corona by a gradual physical process, such as slow magnetic reconnection and flux transport (van Ballegooijen & Martens 1989; Mackay & van Ballegooijen 2001). The flux ropes formed in both of these scenarios may maintain stability for a relatively long timescale prior to the explosive loss of equilibrium (Forbes & Priest 1995; Lin et al. 2004) or a breakout type reconnection that opens up the overlying flux of opposite polarities (Antiochos et al. 1999; Lynch et al. 2004). Such a flux rope is therefore *pre-existing* before its expulsion into interplanetary space. The third picture invokes *in situ formation* of the magnetic flux rope by magnetic reconnection, which also plays the role of violently re-organizing the field configuration in favor of expulsion of the *in situ formed* magnetic flux ropes out of the solar atmosphere. In line with this scenario, several groups have numerically modeled formation of twisted magnetic flux ropes from sheared magnetic arcades by magnetic reconnection that is then erupted (Moore & LaBonte 1980; Mikic & Linker 1994; Demoulin et al. 1996, 2002; Magara et al. 1997; Antiochos et al. 1999; Choe & Cheng 2000). Observationally, formation of the

[1] Physics Department, Montana State University, Bozeman, MT 59717-3840.
[2] Institute of Geophysics and Planetary Physics, University of California, Riverside, CA 92521.
[3] Big Bear Solar Observatory, New Jersey Institute of Technology, Big Bear City, CA 92314-9672.

flux-rope structure during, rather than before, the ejection of CMEs was also suggested by Dere et al. (1999) based on observation of the structures of three CME events and their solar source, and by Demoulin et al. (2002), Nindos & Zhang (2002), and van Driel-Gesztelyi et al. (2003) based on comparison of magnetic helicity budgets in MCs and pre-eruption source regions.

Invoking magnetic reconnection in the mechanism of CMEs re-ignited the decades-old debate on the relationship between flares and CMEs (Sheeley et al. 1983; Cliver et al. 1986; Harrison 1986, 1995; Kahler et al. 1989; Harrison et al. 1990; Kahler 1992; Gosling 1993; Feynman & Hundhausen 1994; Dougherty et al. 2002; Zhang et al. 2002; Andrews 2003; also see Low 1996 and Hundhausen 1999 for reviews). Recent CME observations with LASCO C1-C2-C3 data have demonstrated that the timing relationship between flares and *fast* CMEs is much closer than previously thought (Zhang et al. 2001; Gallagher et al. 2003; Cheng et al. 2003; Wang et al. 2003; Vrsnak et al. 2005), and the latest studies further illustrate a temporal correlation and magnitude scaling relationship between early-stage CME acceleration and the rate of magnetic reconnection inferred from flare observations (Qiu et al. 2002, 2004; Jing et al. 2005; Qiu & Yurchyshyn 2005). These results suggest that magnetic reconnection is an important physical mechanism at least interacting with the trigger and acceleration of the erupting coronal magnetic structures in a good number of CME events, especially those strong, fast, and most geo-effective ones closely associated with solar flares. In particular, depending on specific configurations, solar magnetic flux and helicity may be conveniently converted by reconnection into erupting magnetic flux ropes and carried all the way to 1 AU, making a nonnegligible contribution to the interplanetary flux budget via MCs. With this consideration, a systematic comparison between measurements of magnetic flux involved in low-corona reconnection and the flux inside MC flux ropes will provide crucial new insight into the possible contribution of reconnection flux to the interplanetary flux budget and illuminate the puzzle of flux-rope formation, namely, whether flux ropes are *pre-existing* or *in situ formed*.

This paper presents the first comprehensive study addressing quantitatively the relationship between magnetic flux budgets in low-corona reconnection and the interplanetary flux ropes represented by MCs. We analyze nine events with identified association between flares, CMEs, and MCs and with complete observations in all aspects to allow reliable quantitative measurements. The results of all nine events constitute a reasonable statistical sample for our investigation on the role of magnetic reconnection in transporting solar flux into interplanetary space via magnetic flux ropes, appearing as coronal mass ejections at low corona and magnetic clouds at 1 AU. From an observational point of view, although we do adopt the basic assumption that magnetic reconnection is invoked in the process of eruption for suitable events, we do not assume whether or not reconnection is related to the formation of flux ropes. This important issue awaits testing by the outcome of this study. In the following section, we lay out the framework for the quantitative comparison between magnetic flux budgets in MCs and their solar progenitors, specifically flare ribbons and coronal dimming, as observational tests on various theoretical models concerning the formation mechanisms of magnetic flux ropes. Section 3 gives a brief overview of the observations used in this study. Sections 4, 5, and 6 are dedicated to describing methods of measuring reconnection flux from flare ribbons (Φ_r), MC flux ($\Phi_{t,p}$), and coronal dimming flux (Φ_d), respectively. A quantitative comparison between these measurements is presented in § 7, and the physical implications of our results are discussed in § 8.

2. COMPARISON OF MAGNETIC FLUX BUDGETS

2.1. *Magnetic Reconnection and Flux Rope Formation*

For the purpose of our investigation, it is necessary to revisit several flare-CME configurations that invoke magnetic reconnection to understand how magnetic reconnection flux in low coronae (Φ_r) may be related to magnetic flux in interplanetary flux ropes. In the standard two-dimensional or 2.5-dimensional flare model, also widely known as the CSHKP model (Carmichael 1964; Sturrock 1968; Hirayama 1974; Kopp & Pneuman 1976), reconnection takes place below the pre-existing helical flux rope structure (often embodied by a filament or prominence), and the total amount of flux closed down into postflare loops is identical to the amount of flux closing up into the flux rope. In these pictures, reconnection contributes solely to the incremental poloidal or azimuthal component of the flux-rope flux, while the toroidal or axial component, by which the helical flux rope is anchored to the Sun, is implicitly assumed to be pre-existing (e.g., Lin et al. 2004). Therefore, there is no theoretical association between the toroidal MC flux Φ_t and the low-corona reconnection flux Φ_r, while the measured poloidal MC flux Φ_p at 1 AU should be greater than the reconnected flux. If the pre-existing helix structure contains a significant amount of twisted flux, we expect to find a much greater poloidal flux Φ_p than reconnection flux Φ_r.

In the scenario of in situ formed (by reconnection) magnetic flux ropes, such as in the sheared-arcade model, the helix structure of the flux rope is formed by reconnection, and the entirety of its flux is anchored to the solar surface. In this case, the part of the reconnection flux that is only involved at the two ends of the helical structure is identical to the toroidal flux of the flux rope. This part of the reconnection flux is usually a fraction of the total reconnection flux. Meanwhile, magnetic reconnection would generate twists along the flux rope axis by transporting the mutual helicity in sheared arcades into the self-helicity of the flux rope. The number of twists in the in situ formed flux rope depends on the number of reconnections. In terms of magnetic flux, reconnection flux is comparable to the twisted flux, or the poloidal flux, along the axis. In summary, we expect the total reconnection flux Φ_r to be greater than the toroidal flux Φ_t, but close to and likely proportional to the poloidal flux Φ_p if the helix of the flux rope is dominantly in situ formed.

Note that the poloidal flux Φ_p refers to the integration of the poloidal magnetic field component (the component projected to a plane that is perpendicular to the flux-rope axis) over a cross-sectional area cut along the radius (rather than the diameter, in which case the integration will yield zero net flux) of the flux rope. The so-defined Φ_p is therefore related to the amount of twist along the flux-rope axis and is not independent of Φ_t. Therefore, the so-called "total flux" as a sum of Φ_p and Φ_t is not meaningful. The comparison between reconnection flux (Φ_r) and MC flux (Φ_t and Φ_p) is valid if the ejected helical structure of the flux rope does not change its magnetic morphology during its transit from the Sun to 1 AU. We may safely presume that this condition is met to a large extent, since the corona and interplanetary space are a low-β frozen-in environment.

2.2. *Coronal Dimming*

Coronal dimming, or transient darkening visible in coronal difference images, is often reported to be associated with CMEs (Harrison & Lyons 2000). It is believed to reflect draining of coronal mass along magnetic field lines stretched open during the eruption, thus the dimming areas map the feet of the rising flux rope (e.g., Sterling & Hudson 1997; Webb et al. 2000). Accordingly, for an event on 1997 May 12, Webb et al. (2000)

integrated the longitudinal magnetic flux in dimming areas and found that it was comparable with the toroidal magnetic flux in the associated MC observed at 1 AU 3 days after the coronal event.

On the other hand, Forbes & Lin (2000) and Lin et al. (2004) considered the possibility that coronal dimming areas map the footprints of stretched field lines of the magnetic arcade overlying a pre-existing flux rope, which are then closed down by subsequent magnetic reconnection. In this picture, coronal dimming takes place shortly ahead of magnetic reconnection, and the magnetic flux in dimming regions reflects the total flux added to the poloidal component of the erupting flux rope by reconnection. They believe that when magnetic reconnection proceeds to high corona, it is not energetic enough to produce visible radiation signatures on the solar surface; the magnetic flux encompassed by dimming areas (Φ_d) is therefore a better manifestation of incremental poloidal flux in the flux rope than the ribbon flux Φ_r measured from brightened flare ribbons in the chromosphere. In this scenario, Φ_p is greater than Φ_d, which is still greater than Φ_r. From a different point of view, Mandrini et al. (2005) and Attrill et al. (2006) suggest that the dimming flux Φ_d should be compared with the poloidal MC flux Φ_p or the total MC flux $\Phi_{\rm tot} = \Phi_t + \Phi_p$, arguing that magnetic flux ropes are formed by successive reconnections in a sheared magnetic arcade (Demoulin et al. 1996; Titov & Demoulin 1999). They each presented a case study showing that Φ_d is comparable with Φ_p (Mandrini et al. 2005) or $\Phi_{\rm tot}$ (Attrill et al. 2006) given the length of the MC, $L = 1$ AU.

As an observational test of these various scenarios, it is important to examine the relationship between magnetic fluxes encompassed in dimming areas (Φ_d), flare ribbons (Φ_r), and MCs measured at 1 AU (Φ_t and Φ_p). In this paper, we also present the first quantitative comparison between dimming flux, ribbon flux, and MC flux for a number of events with observations adequate for these measurements.

3. OBSERVATIONS

We study nine events, from 1998 to 2005, with identified association between flares, filaments, CMEs, and MCs. Comprehensive information for these events is given in Table 1. These events are selected from the samples in our previous research as well as published literature. Information on flares and filaments is obtained from an online flare event report,[4] as well as inspection of the coronal observations by the *Transition Region and Coronal Explorer* (*TRACE*; Handy et al. 1999) and the Extreme Ultraviolet Imaging Telescope (EIT; Delaboudinière et al. 1995) and optical observations from the Global Hα network run by Big Bear Solar Observatory (BBSO). Information on CMEs observed by the Large Angle and Spectrometric Coronagraph (LASCO; Brueckner et al. 1995) is obtained from the online LASCO CME catalog.[5]

The association of flare and CME events with magnetic clouds is obtained from six independent sources, including work published in print and online. The most recent of these catalogs only extends to the end of 2003, and so the two events in 2004 and 2005 are determined by the authors. In some cases there was more than one solar event (CME and flare) that could be associated with the magnetic cloud. In those cases, both were considered carefully with further analysis of the location of the flare using EUV full-disk coronal observations from EIT. Table 1 shows the magnetic clouds associated with flares and CMEs and the catalogs from which the identification was sought.

To analyze these events, we collect flare observations in ultraviolet wavelength from *TRACE* and optical wavelength from BBSO. The cadence of the images ranges from a few seconds in *TRACE* observations (typically, 2–4 s, 10 s, and 30 s) to 1 minute in BBSO observations. The time cadence is suitable for our study, as an individual flare ribbon pixel stays flared for a few minutes (see next section). The pixel size of seeing-free *TRACE* observations is $0.5''$, and that of Hα observations is about $1''$. Five-minute averaged longitudinal magnetograms before the flare onset were obtained from the Michelson Doppler Imager (MDI; Scherrer et al. 1995), with a pixel size of about $2''$. Images of the same and different sets were co-aligned with an accuracy of better than $2''$, the MDI pixel size. The flare and magnetic field observations were analyzed to measure the total magnetic reconnection flux as described in the next section. For each event, EIT full-disk images at 195 Å with 12 minute cadence and $2.64''$ pixel size were also collected to investigate the coronal dimming associated with the eruption. The in situ measurements of MC magnetic field and plasma parameters were provided by the *Advanced Composition Explorer* (*ACE*; Smith et al. 1999) spacecraft. MCs were clearly identified by their pronounced features against the solar wind background. These data were fitted with the Grad-Shafranov reconstruction technique, as well as force-free cloud-fitting models, as described in the following sections, to derive the MC flux in both the toroidal and poloidal components.

General characteristics of the nine studied events are listed in Table 1. These events are all associated with halo CMEs (Howard et al. 1982), their mean velocities measured from LASCO C2-C3 observations ranging from 500 to 2500 km s^{-1}. They are associated with C- to X-class flares in the *GOES* categorization, i.e., the soft X-ray radiation output power varies by 3 orders of magnitude. The observed (by C2) launch of the CME and the onset of the flare are within 1 hr for the majority of events. All nine flares are two-ribbon flares, although a few do not exhibit apparent expansion of ribbons. The flare morphology of some events is published in other papers, e.g., the X2.0 flare on 2004 November 7 by Longcope et al. (2007), the M8.0 event on 2005 May 13 by Qiu & Yurchyshyn (2005), and the Halloween event on 2003 October 28 by numerous other authors. Nearly all these events originate from active regions. Four events in this list are associated with erupting filaments, and in five events, filament eruption was not detected, even though filaments were observed in some events (such as in the event on 2005 May 13; Qiu & Yurchyshyn 2005).

4. EVALUATING MAGNETIC RECONNECTION FLUX

The magnetic reconnection rate has been inferred from flare observations by a number of research groups (Poletto & Kopp 1986; Isobe et al. 2002, 2005; Fletcher & Hudson 2001; Qiu et al. 2002, 2004; Fletcher et al. 2004; Qiu & Yurchyshyn 2005; Saba et al. 2006). The measurement is based on the macroscopic picture of magnetic reconnection envisaged in the "standard" flare model, or CSHKP model. The model links the corona reconnection process to observable lower atmosphere signatures, such as flares, as a result of energy release by reconnection, which can be described by the relation (Forbes & Priest 1984)

$$\frac{\partial \Phi_r}{\partial t} = \frac{\partial}{\partial t}\int B_c \, dS_c = \frac{\partial}{\partial t}\int B_l \, dS_l. \quad (1)$$

The left-most term denotes the coronal magnetic reconnection rate, defined by integration of the inflow magnetic field at the corona, B_c, over the reconnection area S_c, or reconnection flux,

[4] See ftp://ftp.ngdc.noaa.gov/STP/SOLAR_DATA/SOLAR_FLARES/XRAY_FLARES/.

[5] See http://cdaw.gsfc.nasa.gov/CME_list/.

TABLE 1

EVENT INFORMATION

EVENT NUMBER	FLARE[a]			FILAMENT INFORMATION[b]	CME[c]		MAGNETIC CLOUD[d]		
	Date	Region	Time and Magnitude		Time	Speed	Date	Start Time	Duration (hr)
1.....	1998 Nov 05	8375	19:55 M8.3	no	20:44	1118	Nov 09	02:00 (L05) 00:00 (L04b) (S03) −05:00 (CR03)	24 (L05) 26 (L04b) (S03) 49 (CR03)
2.....	2000 Jul 25	9097	02:49 M8.0	no	03:30	528	Jul 28	12:00 (CR03)	49 (CR03)
3.....	2000 Aug 09	9114	16:22 C2.3	yes	16:30	702	Aug 12	05:00 (L05) 06:00 (L04b) (L02) (S03) 05:00 (CR03) 06:00 (L04a)	25 (L05) 23 (L04b) (L02) (S03) 41 (CR03) 23 (L04a)
4.....	2001 Apr 10	9415	05:26 X2.3	yes	05:30	2411	Apr 12	16:00 (L05) 08:00 (L04b) (L02) −02:00 (CR03)	15 (L05) 10 (L04b) (L02) 33 (CR03)
5.....	2001 Apr 26	9433	13:12 M7.8	no	12:30	1006	Apr 29	00:00 (L05) 02:00 (L04b) (L02) −10:00 (CR03)	14 (L05) 11 (L04b) (L02) 60 (CR03)
6.....	2003 Oct 28	10486	11:10 X17.	yes	11:30	2459	Oct 29	09:00 (L05)	17 (L05)
7.....	2003 Nov 18	10501	08:31 M3.9	yes	08:50	1660	Nov 20	10:00 (L05)	16 (L05)
8.....	2004 Nov 07	10696	16:06 X2.0	no	16:54	1759	Nov 09	20:40 (Au) (L07)	13.5 (Au) (L07)
9.....	2005 May 13	10759	16:57 M8.0	no	17:22	1642	May 15	05:40 (Au)	23 (Au)

[a] Information is obtained from ftp://ftp.ngdc.noaa.gov/STP/SOLAR_DATA/SOLAR_FLARES/XRAY_FLARES/. Time refers to the peak time, and magnitude refers to *GOES* categorization.

[b] A "yes" indicates filament eruption detected, and a "no" indicates filament eruption not seen.

[c] Information is obtained from http://cdaw.gsfc.nasa.gov/CME_list/. Time refers to when the CME is first observed in LASCO C2 field of view (FOV), and speed, in units of km s^{-1}, refers to the linear fit to the height-time profile obtained from C2-C3 observations.

[d] References not associated with a time or duration indicate the cloud was identified in the referenced list, but no times were given. Negative times relate to the date in the fourth column; e.g., a time of −02:00 refers to a time of 22:00 on the previous day. The events on 2004 November 07 and 2005 May 13 were determined by the authors.

REFERENCES.—(CR03) Cane & Richardson 2003; (L02) Larson 2002; (L04a) Leamon et al. 2004; (L04b) Lepping 2004; (L05) Lynch et al. 2005; (L07) Longcope et al. 2007; (S03) Smith 2003; (Au) Determined by the authors.

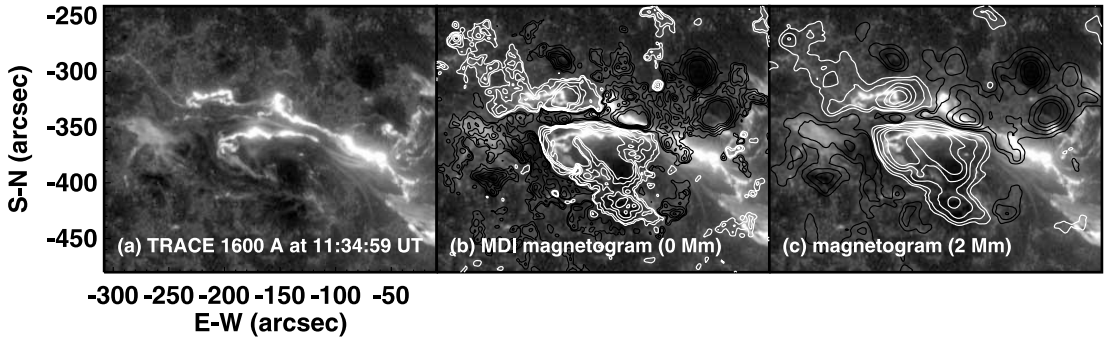

FIG. 1.—(*a*) Snapshot of an X17.2 flare observed at 1600 Å by *TRACE* on 2003 October 28. (*b*) Contours of the photospheric longitudinal magnetogram obtained by MDI, superimposed on a snapshot of the flare observed at 1600 Å by *TRACE*. (*c*) Contours of the longitudinal magnetogram extrapolated to 2 Mm above the photosphere, superposed on the same flare image as in (*b*). The contour levels in panels (*b*) and (*c*) are ±100, 200, 400, 600, and 800 G, and dark and white lines indicate the negative and positive magnetic fields, respectively.

per unit time. On the right-hand side, B_l is the normal component of the magnetic field at the locations of flare patches in the lower atmosphere, which are believed to map the footpoints of field lines reconnecting in the corona, and dS_l is the newly brightened flare area. Directly observing either B_c or S_c at the corona poses insurmountable difficulties with existing technology and instrument capabilities, but B_l and S_l are easily captured in lower atmosphere observations of flares. The relation reflects the conservation of magnetic flux from the coronal reconnection site to the lower atmosphere energy deposit site and is suitable to describe the magnetic reconnection rate in a general configuration, given that evolution of flare brightening reflects the instantaneous lower atmosphere intersection of separatrices along which magnetic reconnection takes place (Hesse et al. 2005). The measurements are valid approximations of the reconnection rate when the following assumptions hold: the photospheric magnetic fields are line-tied, or equivalently, their evolution timescale is much longer than the reconnection timescale; the heating of lower atmosphere during flares is an immediate response to magnetic reconnection at the corona, which transports energy downward along the field lines; and the timescales of magnetic reconnection, energy transport, and heating of the lower atmosphere are shorter than the flare ribbon cooling timescale and observation and/or measurement timescales. Realistically, the timescale of magnetic field evolution ranges from hours to days, and timescales of magnetic reconnection, energy transfer, and atmosphere heating range from a fraction of a second to a few seconds. Meanwhile, the cooling time of flare ribbons in the upper chromosphere or transition region is several minutes, and our observation or measurement cadence is from several seconds to a few minutes. Therefore, the approach is suitable for our purpose.

In this paper, we derive the total reconnection flux Φ_r using an improved semi-automated algorithm. In short, we use flare observations made at optical, UV, and EUV wavelengths to map the footprints of reconnecting magnetic fields. We count all pixels that have brightened during the flare, map them to a coregistered magnetogram, and integrate the signed magnetic flux (Φ_r^+ and Φ_r^-) encompassed by the entire ribbon area. Figure 1 shows an example of measuring flare ribbons and magnetic flux swept up by the ribbons using *TRACE* UV observations of the X17 flare on 2003 October 28. The steps of the measurement are as follows. First, the time series of UV observations from *TRACE* or optical observations from BBSO are co-aligned after correcting the instrument pointing shifts and drifting caused by solar rotation and jittering, using a cross-correlation algorithm, which yields a subpixel co-alignment accuracy. To count ribbon pixels, it is crucial to reliably determine the edge of the newly brightened ribbons. In the present study, we determine that pixels with intensities above N_f times the median background intensity in the quiet region are ribbon pixels. We have experimented on a variety of cutoff values (N_f) with respect to the background intensity in each image normalized to its exposure. The necessity for using a variety of cutoffs is to provide an estimate of the lower and upper limit, or the range, of the measured reconnection flux Φ_r, as there is not a unique cutoff criterion good for all flare events (see also Saba et al. 2006). The lower cut of the ribbon edge is usually just above the plage intensity, and the higher cut should include at least all apparently brightened areas during the peak of the flare, determined via personal inspection. For *TRACE* UV images with very high contrast between flare patches and background, the lower cutoff is around 5, and the higher cutoff can be as high as 15. For Hα images with relatively low contrast, the lower cutoff can be as low as 1.05 and the higher cutoff is usually less than 2. Note that the lower and upper limits determined in our study with such a wide range of cutoff values provide a very conservative estimate of uncertainties. For the studied events, the difference between the lower and upper limit measurements is well within a factor of 2, except for a fairly compact flare on 2000 July 25 (event 2 in Table 2).

Also note that the measurements are performed on running mean images rather than single frames, especially for *TRACE* observations. This is to eliminate transient nonribbon features, such as the projection of transient ejecta visible in some events, some parts of brightened flare loops other than ribbons, and the cosmic-ray contaminations. As these transient features do not survive for more than 1 to 2 frames at any given pixel, they are usually washed out from a running mean image over a few frames. The interval τ used to produce running mean images was determined so that transient features would be significantly weakened, while the ribbon features would remain brightened, i.e., the interval should be shorter than, or comparable with, the cooling time of the ribbon pixels. Figure 2 shows the time history of individual ribbon pixels, illustrating that the typical cooling time is around a few minutes. It is seen that when single-frame images are used to count the ribbon pixels, the transient ejecta feature, brightened pixels due to cosmic rays, and some coronal loop structures are included, and the measured fluxes in positive and negative polarities are fairly unbalanced. When 30 s interval running mean images are used, these transient features are removed, and the flux balance between the two polarities is improved. Another example of an X2.0 flare on 2004 November 7 is discussed in Longcope et al. (2007).

TABLE 2
MAGNETIC RECONNECTION AND CORONAL DIMMING PROPERTIES

	MAGNETIC RECONNECTION FLUX[a]							CORONAL DIMMING FLUX[a,b]	
EVENT NUMBER	Φ_r	R	Flux Range	σ_{mis} (%)	σ_{sat} (%)[c]	Φ_r^0	μ	Φ_d^+	Φ_d^-
1	3.5 ± 0.5	0.8 ± 0.2	2.6 – 4.7	10	...	4.0 ± 0.5	0.88	1.7 ± 0.3 – 3.5 ± 0.6	1.8 ± 0.3 – 4.4 ± 0.8
2	0.7 ± 0.2	1.9 ± 0.5	0.5 – 1.1	14	...	1.0 ± 0.2	1.00	0.3 ± 0.1 – 0.7 ± 0.2	0.6 ± 0.2 – 1.5 ± 0.3
3	2.3 ± 0.5	0.8 ± 0.2	1.5 – 3.3	5	20, 10, 2	2.9 ± 0.6	0.96	0.4 ± 0.1 – 1.5 ± 0.2	0.4 ± 0.1 – 1.3 ± 0.2
4	4.0 ± 0.3	0.9 ± 0.1	3.3 – 4.9	6	2, ..., ...	4.7 ± 0.3	0.96	...	...
5	0.7 ± 0.4	1.5 ± 1.2	0.4 – 1.8	8	...	0.9 ± 0.5	0.88	...	...
6	18.8 ± 1.8	1.2 ± 0.2	15.9 – 22.4	1	6, 2, ...	23.4 ± 2.3	0.91	1.1 ± 0.2 – 3.3 ± 0.4	1.6 ± 0.2 – 5.5 ± 0.8
7	2.5 ± 0.4	0.9 ± 0.2	1.9 – 3.3	5	...	3.6 ± 0.5	0.98	0.8 ± 0.1 – 1.9 ± 0.3	1.6 ± 0.2 – 2.8 ± 0.6
8	4.7 ± 0.5	1.1 ± 0.2	3.7 – 5.9	8	1, ..., ...	6.2 ± 0.6	0.95	2.2 ± 0.3 – 3.1 ± 0.4	1.0 ± 0.2 – 1.6 ± 0.6
9	6.4 ± 0.5	0.9 ± 0.1	5.5 – 7.3	6	1, ..., ...	8.1 ± 0.5	0.96	1.7 ± 0.5 – 3.3 ± 1.4	0.9 ± 0.3 – 1.7 ± 0.5

[a] Magnetic flux in units of 10^{21} Mx.
[b] The coronal dimming flux is obtained with $N_d = 1$ and 1.5, respectively, and the uncertainties reflect the deviation of the measurements with artificial misalignment of 2–4 MDI pixels. See text for details.
[c] The amount (percentage) of possibly underestimated flux due to MDI saturation effect. The numbers given indicate the underestimate (percentage) when using saturation levels of 1500, 1600, and 1700 G, respectively. See details in the text.

The longitudinal magnetogram used to derive the reconnection flux is obtained from MDI and multiplied by a correction factor of 1.56 (Berger & Lites 2003). As flare ribbons occur in the upper chromosphere or transition region, the MDI photospheric magnetogram is extrapolated to $h = 2000$ km above the photosphere using a potential field extrapolation. According to the standard atmosphere model of Vernazza et al. (1981; see their Figs. 1 and 10), we choose $h = 2000$ km as the presumed formation height of the ribbons in the chromosphere, which is nearly the upper limit of the height of the chromosphere. We are aware that the current-free potential field is in general not a good approximation to active regions. However, errors produced by deviation of the realistic field configuration from a potential field are insignificant because of the very low extrapolation height, which is less than 2 MDI pixels, and our procedure for deriving the integral flux, which is not very sensitive to the detailed configuration. A numerical experiment on extrapolating the magnetic field to varying heights of 500, 1000, 1500, and 2000 km using a linear–force-free method with varying values of α (the force-free parameter) from 0 (i.e., potential field) to 0.2 Mm^{-1} shows that a potential-field extrapolation to up to 2000 km would reduce the total integrated flux by about 20% (see Table 2), while a force-free extrapolation with a nonzero α would increase the integrated flux to greater than the flux from the potential-field approximation. Therefore, the photospheric flux integrated over areas encompassed by flare ribbons is an upper limit of Φ_r, and the integrated flux using potential field extrapolation to 2000 km is a lower limit of Φ_r. For uncertainties in the flare-ribbon formation height and field configuration, the mean value of these two limits is used in the following discussion. The signed magnetic longitudinal flux, Φ_r^+ and Φ_r^-, were derived in regions of positive and negative magnetic fields, respectively, and the total reconnection flux Φ_r is the mean of Φ_r^+ and Φ_r^-. Theoretically, the flux in opposite polarities, Φ_r^+ and Φ_r^-, should be identical, as equal amounts of magnetic flux in opposite polarities are involved in magnetic reconnection. However, this is not always reflected in observational measurements (e.g., Fletcher & Hudson 2001). In this study, we evaluate the flux balance by $R = \Phi_r^+/\Phi_r^-$, and Figure 3 shows a plot of R against Φ_r. It is seen that our approach usually yields a good balance between positive and negative fluxes, with R ranging between 0.8 and 1.5, except for one compact event on 2000 July 25 encompassing part of a sunspot (Table 2). The generally good flux balance results from integrating the signed flux from all ribbon pixels without defining a prescribed connectivity, which takes into account the complexity of the magnetic configuration, rather than assuming a simple bipolar geometry (Fletcher & Hudson 2001). This is an important outcome of our improved approach (see also Qiu & Yurchyshyn 2005).

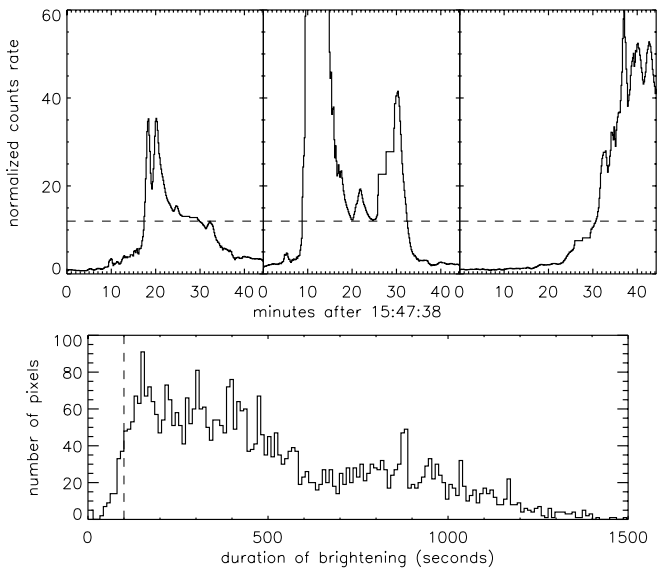

FIG. 2.—*Top*: Intensity profiles of individual flare ribbon pixels with time for the event on 2004 November 7 observed by *TRACE*, showing that flare brightening in an individual ribbon pixel persists for a few minutes. *Bottom*: Histogram of brightening duration for the 4200 ribbon pixels determined using $N_f = 12$ for this event. The dashed line indicates the running mean interval, about 100 s, used for this event.

Uncertainties caused by misalignment between UV/optical flare observations and magnetograms are estimated by artificially offsetting the alignment between the two sets of images by up to 4″, or 2 MDI pixels, which is a very conservative upper limit uncertainty estimate, as the co-alignment accuracy is certainly better than 2″. It is shown that unless flare patches have very small areas and encompass sunspots, the maximum uncertainty by misalignment, σ_{mis}, is about 10% (Table 2). MDI calibration

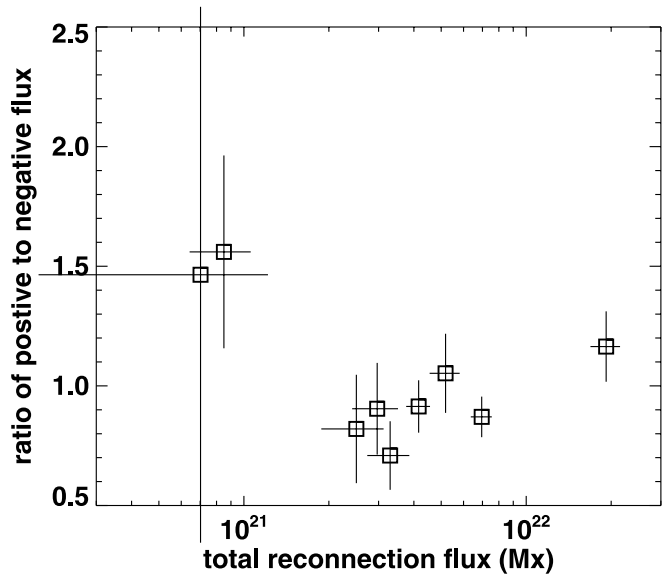

FIG. 3.—Ratio of positive flux to negative flux, $R = \Phi_r^+/\Phi_r^-$, with respect to the mean reconnection flux $\Phi_r = (\Phi_r^+ + \Phi_r^-)/2$.

errors in strong field regions are evaluated using the method by Longcope & Magara (2004) and Longcope et al. (2007). Berger & Lites (2003) reported that MDI measurements saturate the strong field greater than 1700 G. We give an upper limit estimate of such underestimates, $\sigma_{\rm sat}$, due to saturation effects, assuming that saturation takes place at field strengths 1700, 1600, and 1500 G, respectively. For all but one event, flare ribbons do not intrude into regions with field strengths above 1700 G, and in only three events, flare brightenings occur in field strengths above 1500 G, yielding an underestimate of a few percent, at the very maximum, of the total flux (Table 2). Note that the departure of the flux ratio R from unity provides an upper limit estimate of saturation effects, as magnetic flux from the ribbon intruding into the strong field may be underestimated. The generally good flux balance in our measurements indicates that MDI saturation effects are insignificant in this study. Finally, a first-order correction to the projection effect was made by assuming that magnetic fields at flare ribbons are radial, and Φ_r is therefore corrected by the cosine (μ) of the position angle of the flare region. As all events in this study occur at or near the disk center, the projection effect is insignificant.

Table 2 lists relevant information for the reconnection flux measurements, including the upper and lower ranges of these measurements, the uncertainties caused by misalignment ($\sigma_{\rm mis}$), underestimates of flux due to saturation effects ($\sigma_{\rm sat}$), and the flux (Φ_r^0) measured using a photosphere magnetogram, i.e., without extrapolation. Our improved algorithm allows us to perform the most comprehensive evaluation of measurement uncertainties from a variety of sources. We note that these estimates all reflect the upper limits of uncertainties caused by various sources. Ultimately, the reconnection flux Φ_r of each event is the mean value of measurements using a range of combinations of N_f and τ, as well as alignment offsets, and the uncertainties quoted in the table are a combination of standard deviations from these measurements.

5. MEASURING MAGNETIC FLUX IN MAGNETIC CLOUDS

The interplanetary counterparts of the aforementioned flare-associated CMEs, the ICMEs/MCs, were examined by two means. One is the so-called Grad-Shafranov (GS) reconstruction technique (e.g., Hu & Sonnerup 2002), which is to derive a 2.5-dimensional cross section of a cylindrical flux rope from a single in situ spacecraft measurement. There is no prescription for the geometry of the cross section and no assumption about the force-free condition. Therefore, both the magnetic field and plasma data have to be used. The other is the conventional model fitting by the axisymmetric force-free Lundquist solution (Lundquist 1950) to the in situ spacecraft data (e.g., Lepping et al. 1990; Leamon et al. 2004; Lynch et al. 2005). This is sometimes advantageous when only limited spacecraft measurements are available. We are aware of certain variations on this approach, such as those with non–force-free magnetic field profiles and/or noncircular cross sections (e.g., Mulligan & Russell 2001; Hidalgo et al. 2002). However, they all follow the same path by using a predetermined "global" configuration to fit the one-dimensional data, whereas the GS method uses the one-dimensional data as initial values to derive a fully two-dimensional solution with a more sophisticated theoretical basis. Moreover, the GS method offers better control in assessing the validity of the results, as is briefly discussed below. Both methods are deemed valuable and sometimes complementary to each other. Thus, both methods are utilized in this paper, which also provides a means to test the robustness of the MC flux measurements. A general comparison between different techniques was presented by Riley et al. (2004), and further discussion is given in this paper, based on our nine case studies.

5.1. *Grad-Shafranov Reconstruction*

The GS reconstruction technique is based on the Grad-Shafranov equation (Sturrock 1994; Hau & Sonnerup 1999). In a Cartesian coordinate system, (x, y, z), it is written

$$\frac{\partial^2 A}{\partial x^2} + \frac{\partial^2 A}{\partial y^2} = -\mu_0 \frac{dP_t}{dA}, \tag{2}$$

which describes two-dimensional ($\partial/\partial z \approx 0$, where z is the axis of a cylindrical flux rope, for instance) magnetic and plasma structures in quasi-static equilibria in a proper frame of reference. The magnetic field is $\boldsymbol{B} = (\partial A/\partial y, -\partial A/\partial x, B_z(A))$, which satisfies $\nabla_t A \cdot \boldsymbol{B}_t = 0$, implying that the equal-value contours of A represent transverse magnetic field lines, $\boldsymbol{B}_t = (B_x, B_y)$. On the right-hand side, the single-variable function $P_t(A)$ is the sum of the plasma pressure $p(A)$ and the axial magnetic pressure $B_z^2(A)/2\mu_0$. Both are functions of A alone. This important feature of sole dependence on A enables us to determine the z-axis orientation and check the validity of the locally two-dimensional assumption (for details, see Hu & Sonnerup 2002; Hu et al. 2004).

In a frame of reference that is moving with the structure, usually the deHoffmann-Teller (HT) frame, in which the electric field vanishes, the spacecraft is traversing the structure with velocity $-\boldsymbol{V}_{\rm HT}$. Here the frame velocity $\boldsymbol{V}_{\rm HT}$ is determined from spacecraft measurements (Khrabrov & Sonnerup 1998), the property of which is useful for assessing the static nature of the structure. From the spacecraft data along $y = 0$ (the x-axis, i.e., the projected spacecraft path onto the transverse plane), we obtain $A(x, 0) = -\int_0^x B_y(\zeta, 0)\, d\zeta$, $d\zeta = -\boldsymbol{V}_{\rm HT}\hat{\boldsymbol{x}}\, dt$, and $P_t(x, 0) = p(x, 0) + B_z^2(x, 0)/2\mu_0$. An analytic function $P_t(A)/B_z(A)$ is then applied to fit $P_t(x, 0)/B_z(x, 0)$ versus $A(x, 0)$. The right-hand side of GS equation (2) is explicitly known. The GS equation is then solved to obtain $A(x, y)$ in a rectangular domain. Finally, the 2.5-dimensional magnetic field structure, $B_x(x, y)$, $B_y(x, y)$, and

TABLE 3
MEASUREMENTS OF MAGNETIC CLOUD PARAMETERS FOR THE EVENT ON 2004 NOVEMBER 9–10

Parameter	Lundquist Fitting	GS Method
θ_0 (deg)	-44.8 ± 20	-22
ϕ_0 (deg)	265.8 ± 3.8	218
B_0 (nT)	33.41 ± 2.66	43
R_0 (Gm)	13.96 ± 2.51	...
Y_0/R_0 (AU)	0.07 ± 0.06	-0.042
χ^2/B_0^2	0.03	...
H	-1	-1
Φ_t (Mx)	$(8.83 \pm 3.88) \times 10^{20}$	6.4×10^{20}
Φ_p (Mx)	$(29.09 \pm 7.5) \times 10^{20}$	35×10^{20}

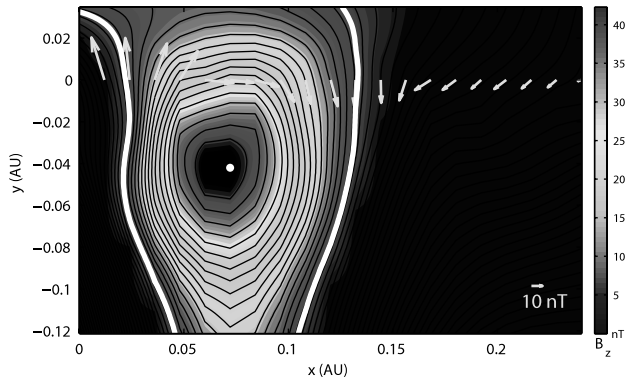

FIG. 4.—Illustration of the GS reconstruction method applied to the MC observed by *ACE* during 2004 November 9–10. The black contour lines are transverse magnetic field lines. The colors represent the axial magnetic field (B_z) distribution as indicated by the colorbar. The arrows are the measured transverse magnetic field vectors along spacecraft path ($y = 0$; scales given by the arrow in the lower right corner denoted by 10 nT). The thick white contour line and the circle denote the boundary and the center of the flux rope, where $A = A_b$ and $A = A_m$, respectively. [*See the electronic edition of the Journal for a color version of this figure*.]

$B_z(A(x, y))$, is reconstructed. It yields an exact fit of the model solution to the spacecraft magnetic field measurement along its path ($y = 0$). The recovered magnetic flux rope structure is composed of nested cylindrical isosurfaces of $A(x, y)$ that carry helical field lines winding along the z-axis. The method has been extensively tested by exact solutions to model GS equations (e.g., Hu & Sonnerup 2002; Hu et al. 2003) and by utilizing multi-spacecraft data (e.g., Hu et al. 2005; Hasegawa et al. 2004). In particular, a recent GS reconstruction by Sonnerup et al. (2004) of a small-scale flux rope (a flux transfer event) at Earth's magnetopause showed excellent agreement between the GS numerical solution and the actual spacecraft measurements among all four *Cluster* satellites.

Subsequently, the toroidal (axial) magnetic flux can be calculated as $\Phi_t = \int\int B_z\, dx\, dy$ within a certain boundary defined by $A = A_b \equiv$ const. The poloidal magnetic flux Φ_p is $|A_m - A_b|L$, where A_m corresponds to the A value at the center of the flux rope and L is the length of the flux rope in the z-dimension. The boundary $A = A_b$ is chosen such that the requirement that $P_t(A)$ and/or $B_z(A)$ be single-valued is violated for either $A > A_b$ or $A < A_b$ outside of the boundary. In other words, such a boundary encloses a domain within which the two-dimensional cylindrical assumption remains valid, as judged from the spacecraft data.

Correspondingly, the aforementioned two quantities can also be evaluated with Lundquist fitting by analytical formulae, with the definition of the boundary as the circular surface where $B_z = 0$ (e.g., Leamon et al. 2004; Lynch et al. 2005). We are aware that there is an uncertainty in estimating L. In this study, we take $L = 1$ AU, or calculate the poloidal flux per AU, while taking $L = 0.5$ AU as the lower limit (e.g., DeVore 2000) and $L = 2$ AU as the upper limit (e.g., Nindos et al. 2003). The uncertainty in the flux-rope length is further discussed in § 5.3.

5.2. *Force-Free Cloud Fitting Method*

In this paper, we also present the MC magnetic flux calculated using the technique of Leamon et al. (2004). This is based on an earlier paper by Lepping et al. (1990) and uses the constant-α force-free cylindrical symmetric solution of Lundquist (1950). In cylindrical coordinates, there are $B_t = B_0 J_0(\alpha r)$, $B_p = HB_0 J_1(\alpha r)$, and $B_r = 0$, where B_t, B_p, and B_r are the toroidal (axial), poloidal (azimuthal), and radial components of the magnetic field, respectively, B_0 is the magnetic field strength along the axis of the cylinder, $H = \pm 1$ is the handedness of the flux rope, where plus and minus indicate right and left handedness, respectively, and J_n are the nth order Bessel functions. The force-free parameter α is given as $\alpha = 2.4048/R_0$, where 2.4048 is the location of the first zero of J_0. The technique of Leamon et al. (2004) compares the modeled magnetic field $\boldsymbol{B}^M$ with that of the observed field $\boldsymbol{B}$ and uses the downhill simplex method (Nelder & Mead 1965, with a variety of starting points and an appropriate determination of H from observing the data) to minimize $\chi^2 = (1/3N)\Sigma\left|\boldsymbol{B} - \boldsymbol{B}^M\right|^2$. This returns the following parameters for the modeled magnetic cloud: θ_0 and ϕ_0, the latitude and longitude of the cloud axis, R_0 and B_0, the radius and magnetic field strength of the cloud, Y_0, the impact parameter, or distance of the spacecraft from the cloud axis at closest approach, t_0, the time of closest approach to the spacecraft, and χ^2, an indicator of the goodness of fit of the model to the data.

Uncertainties for each parameter were determined using the technique produced by Lepping et al. (2003). This employs results obtained by comparing the model of a simulated cloud along with a noised-up version of the same cloud. This prescription (§ 5 of Lepping et al. 2003) combines $\sqrt{\chi^2}$, Y_0, and cone angle $\beta_{\rm ca}$ ($\cos\beta_{\rm ca} = \cos\theta_0 \cos\phi_0$) and produces σ-values for each of the modeled parameters. An additional uncertainty can be produced for R_0 by estimating the cloud's diameter using the duration of the spacecraft passage through the cloud, ΔT, as $R_{\Delta T} = \left[Y_0^2 + (\sin\beta_{\rm ca} V_c \Delta T/2)^2\right]^{1/2}$, where V_c is the cloud speed. The uncertainty of R_0 in the present report is hence the combination of both σ_{R_0} and the difference between $R_{\Delta T}$ and R_0.

The magnetic flux magnitudes within the cloud in the toroidal and poloidal components are given by

$$\Phi_t = \frac{2\pi J_1(x_{01})}{x_{01}} B_0 R_0^2, \quad \Phi_p = \frac{L}{x_{01}} B_0 R_0, \tag{3}$$

where x_{01} is the first zero of the Bessel function J_0 ($\sim$2.4048) and $J_1(x_{01})/x_{01} \sim 0.21588$ (e.g., Lynch et al. 2005). L is the total length of the cloud, assumed to be 1 AU (or 150 Gm) in this study. An example of a fitting to the MC to obtain relevant parameters, as well as error estimates, is given in Table 3 for the event on 2004 November 9–10.

Figures 4 and 5 show the fitting results for the MC during 2004 November 9–10, using the GS reconstruction and force-free model fitting techniques, respectively. Results for the nine studied events using both techniques are presented in Table 4. Because of our focus on the poloidal and toroidal flux in MCs, only B_0, R_c (when applicable), Φ_p, and Φ_t are presented. For reference, we also list the results for some events reported by Lynch et al. (2005),

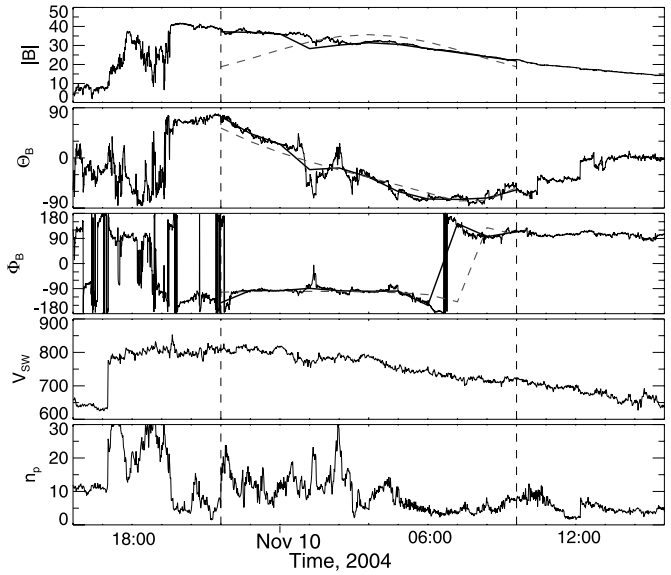

FIG. 5.—Illustration of the force-free model fitting results for the MC event on 2004 November 9–10. From top to bottom, the plots show the magnitude of the magnetic field (in units of nT), latitude and longitude of the cloud axis, the solar wind speed (km s^{-1}), and proton density (cm^{-3}), measured in situ during the passage of the *ACE* spacecraft. The nonvertical dashed lines show the model fitting results superimposed on the measurements.

also using a force-free cloud fitting method. The comparison between these results will be discussed in the last section.

5.3. *Uncertainties in MC Flux Measurement*

Different models will yield different results. For example, the flux-rope axis orientations obtained from the model fitting and the GS method can sometimes differ by tens of degrees (Hu & Sonnerup 2002; Leamon et al. 2004). Generally speaking, there are smaller deviations in integrated quantities, such as the total axial current and magnetic flux (the latter being illustrated in Fig. 8; see also Leamon et al. 2004). For instance, the geometry of the cross section of the 2004 November 9–10 magnetic cloud, as shown in Figure 4, obtained from the GS method is not of the circular shape as prescribed by the Lundquist model. However, the fluxes obtained from both methods agree fairly well. On the other hand, the measured flux largely depends on the area (the radius for the Lundquist model) of the flux-rope cross section, which in turn is primarily affected by the size of the chosen interval and the flux-rope axis orientation. Significant deviations may occur, sometimes mainly due to the different selection of flux-rope intervals. The GS method relies on a more strict criterion to choose the flux-rope interval (as described in § 5.1), which often yields a smaller interval than used by the force-free cloud fitting method and thus may not enclose all the relevant fluxes contained in an MC. This can be seen in Figures 8*b* and 8*c* (shown below), where in most cases, measurements by GS reconstruction (*red symbols*) are smaller than the corresponding measurements by fitting to Lundquist solutions (*blue and green symbols*). We speculate that for some events, the GS method probably provides a lower bound of the fluxes, whereas the model fitting gives an approximate upper bound, especially considering that the Lundquist model assumes a circular cross section.

In a recent study, Dasso et al. (2006) compared magnetic cloud fitting results using both the traditional model-fitting method with four different models based on different approximations on the magnetic field configuration, and a new model-independent direct method to determine the magnetic cloud boundary. It was found that with two different analysis methods, minimum variance analysis and simultaneous fitting, applied to four different models for the event studied in their paper, the maximum deviation from the mean value is 18% in the axial (toroidal) flux and 25% in the azimuthal (poloidal) flux per AU, and the change of the boundary has an effect comparable to these values. We also note that the model-independent direct method by Dasso et al. (2006) yields smaller fluxes and helicity associated with the flux rope than those estimated from fitting models, but the total poloidal flux of the original flux rope before reconnection with solar wind is greater (than model-fitting results) by less than a factor of 2, and the change in the toroidal flux is insignificant. In comparison, in our study, the uncertainties come up as large as comparable to the mean values of the fluxes in each event (see Table 4 and Fig. 8). This is mainly caused by our varying the cloud intervals in a large range to be conservative. Compared with the comprehensive analysis using methods by Dasso et al. (2006), the uncertainties contributed by averaging results from different fitting models and varying cloud boundaries as reported in our measurements should therefore be conceived as the very upper limits.

The largest uncertainty in the MC flux measurement stems from the hardly fathomed length of the MC flux rope. All existing cloud-fitting algorithms using the in situ one-dimensional satellite measurements treat the flux rope as a two-dimensional cylindrical structure. Therefore, to the best extent, we can only obtain the poloidal flux or twist per unit length, such as per AU. To date, only one study (Larson et al. 1997) has attempted to assess the "real" length of the flux rope by evaluating the time of flight of

TABLE 4
MAGNETIC CLOUD PROPERTIES

	GRAD-SHAFRANOV METHOD[a]			FORCE-FREE MODEL FITTING[a,b]				FORCE-FREE MODEL FITTING[a,c]			
EVENT NUMBER	B_0	Φ_t	Φ_p	B_0	R_c	Φ_t	Φ_p	B_0	R_c	Φ_t	Φ_p
1	25	0.96	2.8	17.70 ± 3.83	22.47 ± 3.73	1.21 ± 0.66	2.48 ± 0.95	17.5	18.75	0.8	2.1
2	15	0.07	0.55	15.3 ± 2.7	13.8 ± 10.0	0.4 ± 0.6	1.3 ± 1.2	...	...	...	...
3	35	0.76	2.00	26.32 ± 2.66	26.67 ± 6.45	2.54 ± 1.48	4.38 ± 1.50	29.1	22.5	2.0	4.1
4	21	0.16	0.58	9.04 ± 0.76	45.93 ± 17.62	2.59 ± 2.20	5.18 ± 3.42	8.1	7.1	0.1	0.4
5	21	0.14	0.65	10.78 ± 1.28	17.65 ± 9.44	0.46 ± 0.54	1.19 ± 0.78	11.5	12.2	0.2	0.9
6	47	5.4	12.	42.04 ± 4.36	68.29 ± 24.4	26.6 ± 21.7	17.9 ± 8.24	43.5	37.8	8.4	10.3
7	57	0.64	4.8	43.49 ± 6.59	15.66 ± 11.31	1.45 ± 2.31	4.25 ± 3.71	42.9	15.8	1.4	4.2
8	43	0.64	3.5	33.41 ± 2.66	13.96 ± 2.51	0.88 ± 0.39	2.91 ± 0.76	...	...	...	...
9	53	2.1	4.2	56.14 ± 13.7	49.34 ± 9.44	18.54 ± 11.61	17.28 ± 7.52	...	...	...	...

[a] The units of B_0, R_c, and magnetic flux are nT, GM, and 10^{21} Mx, respectively, and the value of Φ_p refers to the flux per AU.
[b] See text for obtaining uncertainties.
[c] From Lynch et al. (2005).

suprathermal electrons spiraling along the field lines into interplanetary space. Their study provides $L = 2.5$ AU, which can be regarded as the very upper limit of L, in which case the flux rope would carry the same (large) amount of twist along its entire length. Generally speaking, when bidirectional electrons are observed in interplanetary clouds, it is quite possible that the MCs are still rooted on the Sun, when observed at 1 AU (Richardson 1997; Shodhan et al. 2000). In such a case, L can be as large as 2 AU. On the other hand, an independent case study combining observational measurements and theoretical modeling for one event on 2004 November 7–10 (event 8 in our list), Longcope et al. (2007) show that the total magnetic helicity transported from sheared arcades into the flux rope by low-corona reconnection agrees well with the magnetic helicity in the associated MC by taking $L = 1$ AU. Given the current state of research in this field, we take the value of 0.5 AU as the lower limit of L (DeVore 2000) and 2 AU as the upper limit of L (Nindos et al. 2003). Such choices of the lower and upper limits of L would change Φ_p to vary between half and twice the measured values.

6. CORONAL DIMMING

In conjunction with measurements of Φ_r and $\Phi_{t,p}$, we also study EIT full-disk coronal observations to derive coronal dimming areas and the magnetic flux Φ_d encompassed in these areas. For each event, we employ EIT images of 12 minute cadence and 8 hr time range around the time of the eruption, starting 2–3 hr before the onset of eruption or flare. EIT images are calibrated using the standard SolarSoftware packages with solar rotation effects removed and an algorithm designed to find the dimming regions, as well as estimate uncertainties in the measurements.

Following the convention with imaging observations of the corona, the dimming region is found to have a significant post-eruption intensity drop lasting for at least half an hour. Several criteria are employed to define the intensity drop. First, intensity light curves are produced for each pixel, and a pixel is regarded as reflecting a dimming signature when the intensity drop relative to the pre-eruption intensity in the same pixel is greater than $3\sigma_q$, where σ_q is the relative standard deviation of the intensities in an undisturbed (quiescent) region, and the absolute intensity during the dimming is below N_d times the mean quiescent Sun intensity I_q. The measured dimming pixels are mapped to co-aligned MDI longitudinal magnetograms, and the magnetic flux integrated in dimming regions is derived as the dimming flux Φ_d. Note that we multiply the magnetic flux density measured by MDI by a factor of 1.56 as a first-order correction to MDI measurements (Berger & Lites 2003). Given the MDI noise level and the fact that coronal dimming mostly occurs in weak field regions, we also filter out the flux density smaller than 10 G.

As coronal dimmings are large scale signatures and do not exhibit sharp contrast with respect to the background, as in the case of flare brightenings, there is a large uncertainty in determining the edges of dimming regions. To get around this difficulty, we vary N_d between 1 and 2 to derive the range (uncertainty) of the dimming area measurements, which yields about half an order of magnitude variation in the measured Φ_d. Similar to § 4, artificially offsetting the co-alignment between EIT and MDI images by up to 4 EIT pixels (or $\sim 10''$) gives a conservative estimate of measurement uncertainties due to misalignment.

For the nine events reported in this study, dimming measurements are performed in eight events with available post-eruption EIT observations suitable for the measurements. Dimming is detected in seven events. Figures 6 and 7 show dimming flux measurements in two examples, event 2 (2000 July 25) and event 9 (2005 May 13). The figures show pre- and post-eruption EIT images, the difference image between the two, and the map of measured dimming regions at various locations with $N_d = 1$, superimposed on the pre-eruption MDI magnetogram and in comparison with flare-ribbon areas. Also given are time profiles of the mean intensity of the dimming regions, in comparison with the profiles of quiescent Sun and coronal hole intensity (coronal holes are determined as the dimmest pixels in the disk using 10 frame-averaged pre-eruption EIT images). In a couple of events, the absolute intensity in some dimming regions drops to the coronal hole level, while the intensity of most other regions/events, although exhibiting significant relative drop, does not drop as low as coronal hole intensity.

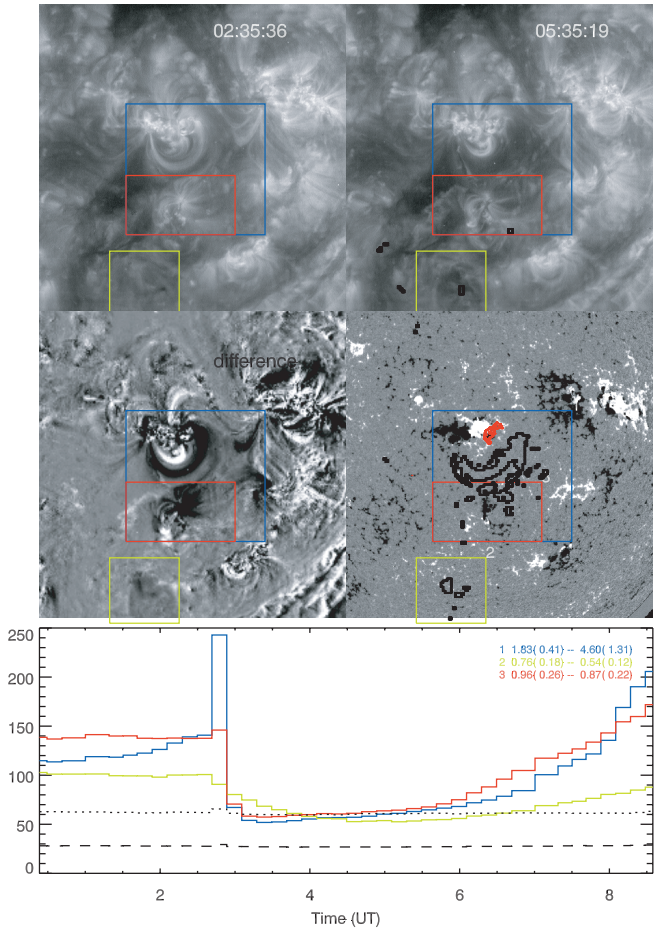

FIG. 6.—Analysis of coronal dimming for event 2 (on 2000 July 25). *Top*: Calibrated EIT intensity images before and after the eruption. *Middle left*: Difference image between pre- and post-eruption images shown in the top panel. *Middle right*: MDI longitudinal magnetogram superposed with flare ribbon areas (*red contours*) and coronal dimming areas (*black contours*). *Bottom*: Intensity time profiles of coronal dimming regions in comparison with the light curves of coronal holes (*dashed lines*) and quiescent regions (*dotted lines*). Boxes in different colors in the top and middle panels indicate different locations where corona dimming flux is measured, and the intensity light curves of coronal dimming measured at these different locations are plotted in the same colors in the bottom panel. This figure shows coronal dimming areas determined with $N_d = 1$ (see text).

In the studied events, coronal dimming occurs shortly after the eruption and usually occupies a larger area than flaring patches at the outskirts of the flare site. Some events, such as the event on 2005 May 13 (Fig. 7), exhibit evident post-eruption coronal dimming judged from EIT original and difference images, but in a few events, some apparent dimming features (such as in regions 1 and 3 in Fig. 6) found by the algorithm resemble coronal loop structures, which are projected onto the disk before the eruption

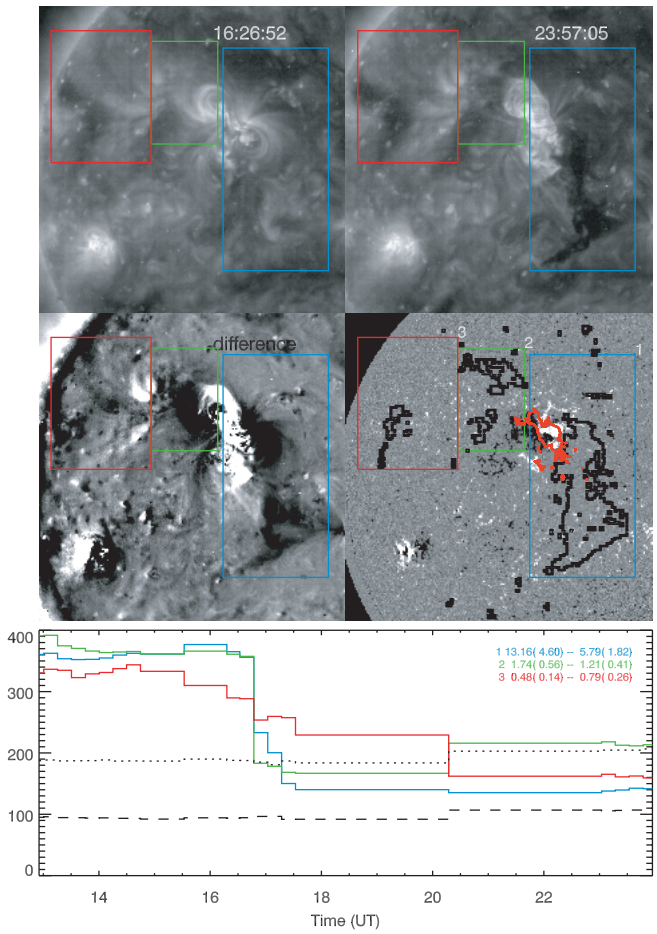

FIG. 7.—Same as Fig. 6, but for event 9 (on 2005 May 13).

and reoriented after the eruption. The apparent removal of active region loops projected onto the solar disk doubtlessly provides a major source of overestimating Φ_d. Therefore, to the best of our knowledge, Φ_d measured from imaging observations usually reflect an overestimate of the dimming flux.

The last two columns in Table 2 give measurements of Φ_d in positive and negative polarities, respectively, as there is usually not a good balance between Φ_d^+ and Φ_d^-, probably because of many large unknown uncertainties involved in the measurements. The Φ_d^+ and Φ_d^- listed in the table are values at $N_d = 1$ and 1.5, and quoted errors merely reflect the standard deviation of a set of measurements with varying alignment offsets. In the following sections, the mean value of Φ_d measured with $N_d = 1$ and 1.5 is compared with Φ_r and $\Phi_{t,p}$, with the notion that Φ_d is an overestimate (sometimes by a large amount) of the dimming flux.

7. MAGNETIC FLUX BUDGETS

The key results for the nine studied events are listed in Table 2 (the reconnection flux Φ_r and the dimming flux Φ_d) and Table 4 (the MC flux in toroidal and poloidal components Φ_t and Φ_p). A direct comparison between these measurements is given in Figures 8 and 9. In Figure 8, $\Phi_{t,p}$ obtained from all three independent methods are presented in different colors, and the mean value of the three measurements is given by dark symbols. Estimates of uncertainties ($\sigma_{t,p}$) in measuring $\Phi_{t,p}$ with the cloud-fitting algorithm by Leamon et al. (2004) are obtained with the method described in § 5, but this method is not implemented in the Grad-Shafranov algorithm and in Lynch et al. (2005); hence we assign the same amount of uncertainties in the MC flux measurements from all three methods. Uncertainties in Φ_r and Φ_d quoted in the tables and figures are obtained as described in the last sections.

For all these events, the poloidal MC flux Φ_p (with $L = 1$ AU) is rather large with respect to the toroidal flux Φ_t (Fig. 8*a*). This is in agreement with Lynch et al. (2005). Note that by definition, Φ_p indicates the amount of magnetic twist along the flux rope axis per AU. These results in general suggest that magnetic clouds are highly twisted flux ropes. The comparison between reconnection flux and MC flux in both the poloidal and toroidal components is given in Figures 8*b* and 8*c*. The figure reveals that the toroidal MC flux Φ_t is usually a fraction of the reconnection flux Φ_r. In comparison, the poloidal MC flux Φ_p is comparable to Φ_r, with their ratio close to unity (when $L = 1$ AU). The figure further suggests a proportionality between the independently measured reconnection flux and MC flux for the studied events. Listed in Table 5 are the linear cross-correlation ρ between the paired data

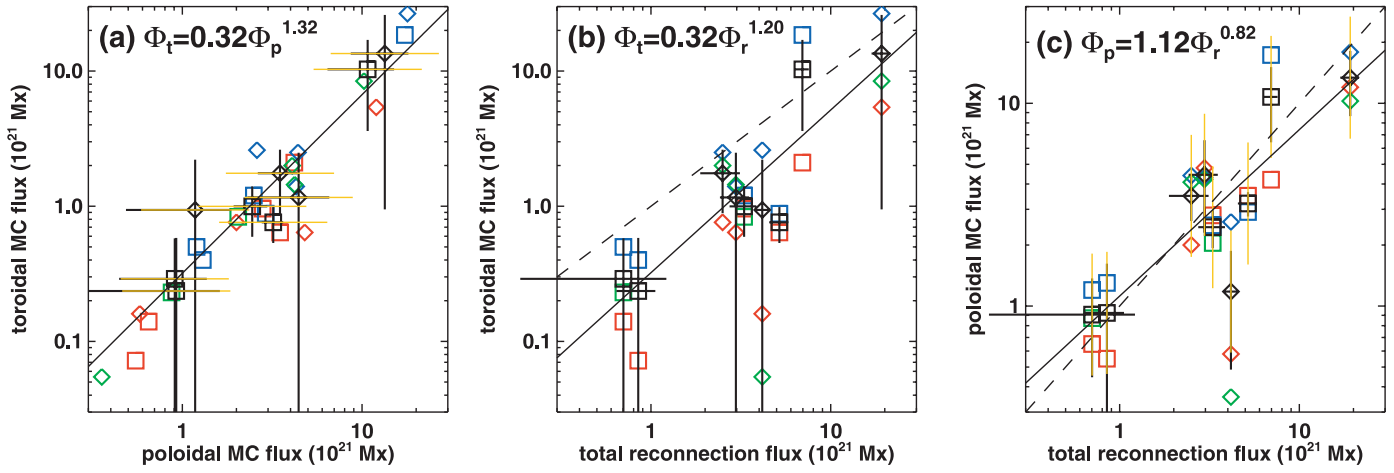

FIG. 8.—(*a*) Toroidal vs. poloidal magnetic flux in MCs, (*b*) toroidal MC flux vs. total reconnection flux, and (*c*) poloidal MC flux vs. total reconnection flux in nine events. Squares indicate events associated with filament eruption, and diamonds indicate events without filament eruption. Red, blue, and green symbols indicate MC flux measurements by GS method, force-free cloud-fitting method by Leamon et al. (2004), and force-free cloud-fitting method by Lynch et al. (2005), respectively. The mean values of the MC flux measurements from the three models are given by dark symbols, with the dark bars indicating uncertainties from these three measurements. Note that the MC poloidal flux refers to the measurements using $L = 1$ AU, and the orange bars in panels (*a*) and (*c*) indicate the range of the poloidal flux by taking $L = 0.5$ AU as a lower limit and $L = 2$ AU as an upper limit (see text). The solid lines in each panel show the linear least-squares fit to data pairs in logarithmic scales, with the fitting results marked in the figure. The dashed lines in panels (*b*) and (*c*) indicate $\Phi_y = \Phi_x$.

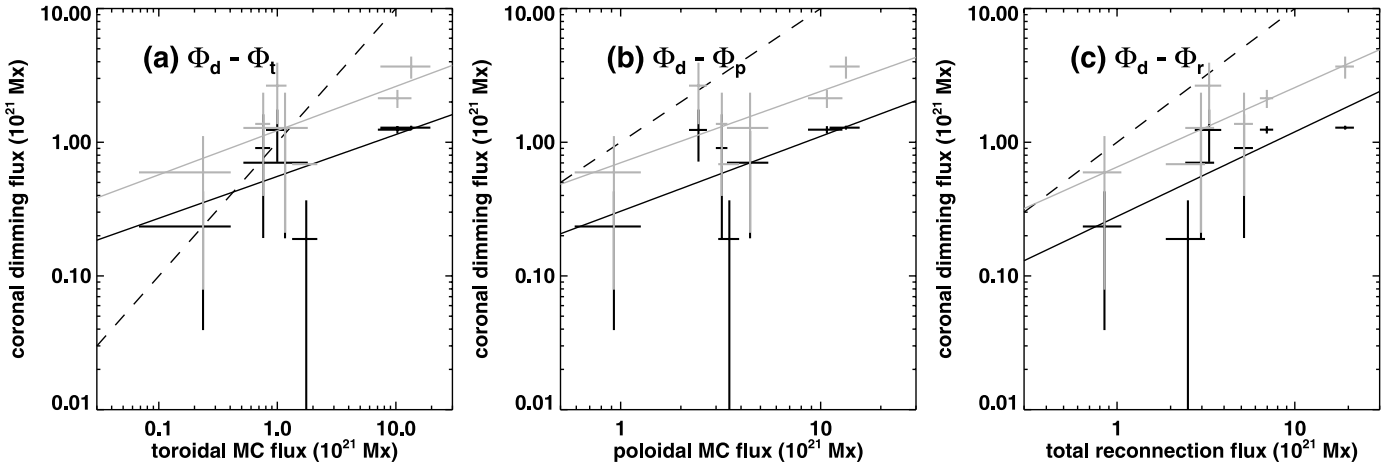

FIG. 9.—Coronal dimming flux vs. (*a*) toroidal MC flux, (*b*) poloidal MC flux, and (*c*) total reconnection (ribbon) flux in seven events. Dark and gray symbols indicate measured Φ_d with $N_d = 1$ and 1.5, respectively. The solid lines show the linear least-squares fit to data pairs in logarithmic scales. The dashed lines indicate $\Phi_y = \Phi_x$.

points, and the confidence level *P*. In general, a good correlation with $P > 99\%$ is presented between the reconnection flux and MC flux in either component. As the Halloween event exhibiting the largest reconnection flux, as well as MC flux, dominates the cross-correlation computation, we also list ρ and *P* computed for eight events without taking into account the fluxes for the Halloween event. The confidence level for these eight data sets remains greater than 95%.

A more quantitative evaluation of the flux relationship can be reflected by the least-squares fit to the data pairs in logarithmic scales, i.e., $\Phi_y \sim \Phi_x^{\gamma}$, and the solid lines superposed in each plot in Figures 8 and 9 indicate the best fit to the data. The results from the fits are as follows:

$$\Phi_t \approx (0.32 \pm 0.09)\Phi_p^{(1.32\pm0.19)},$$
$$\Phi_t \approx (0.32 \pm 0.12)\Phi_r^{(1.20\pm0.25)},$$
$$\Phi_p \approx (1.12 \pm 0.34)\Phi_r^{(0.82\pm0.20)},$$

yielding the power-law index γ close to unity, with the uncertainties in the parameters directly obtained from the fitting procedures. On average, the ratio of Φ_p to Φ_r is around unity when taking $L = 1$ AU. With $L = 0.5$ AU as the lower limit, this ratio becomes half, i.e., the total MC poloidal flux would become about 55% of the reconnection flux, and with $L = 2$ AU as the upper limit, the reconnection flux would contribute about 45% to the total poloidal flux in the MC. Therefore, within the uncertainties, these results can be summarized as $\Phi_r \approx \Phi_p$, $\Phi_r > \Phi_t$, and $\Phi_r \propto \Phi_{p,t}$, namely, the low-corona reconnection flux is comparable to the poloidal MC flux, greater than the toroidal flux (by at least a factor of 2), and proportional to either. Such a relationship indicates that the magnetic flux and twist in interplanetary flux ropes, here specifically the magnetic clouds observed and measured in situ at 1 AU, are highly relevant to low-corona magnetic reconnection.

Note also that with our limited samples, the Φ_p-Φ_r diagram does not exhibit a bimodal pattern to distinguish events associated with filament eruption from those without filament eruption. In other words, events associated with filament eruption do not necessarily possess a greater Φ_p-to-Φ_r ratio than events without filament eruption. Therefore, erupting filaments do not seem to carry significant pre-existing flux in our samples. In short, the result that Φ_r is greater than Φ_t but comparable and proportional to Φ_p, regardless of the presence of filament eruption, complies with the scenario in which the helical flux rope is largely in situ formed by magnetic reconnection in low-corona immediately before its expulsion into interplanetary space.

In Figure 9, we also present measurements of the coronal dimming flux Φ_d, when applicable, in comparison with the ribbon flux Φ_r and MC flux $\Phi_{t,p}$. Coronal dimming can be detected in seven events. The dimming flux Φ_d in the figure is the mean of the positive and negative flux, measured with $N_d = 1$ and 1.5, respectively. The measured dimming flux for these events is at the low end of 10^{21} Mx. It is seen that the dimming flux Φ_d is comparable with the toroidal MC flux Φ_t, in an order-of-magnitude sense, and systematically smaller than the poloidal MC flux Φ_p, as well as the ribbon flux Φ_r. As the measured Φ_d is considered to be the upper limit, Φ_d makes only a fraction of Φ_r or Φ_p for the studied events. Therefore, if Φ_d were associated with Φ_p for any reason, the contribution would be significantly smaller than Φ_r measured from brightened flare ribbons. This is discussed further in the next section.

8. CONCLUSIONS AND DISCUSSION

The total magnetic flux in MCs is believed to originate from the Sun. Therefore, the footprints of the CME magnetic field

TABLE 5
CROSS-CORRELATION AND CONFIDENCE LEVEL BETWEEN Φ_t, Φ_p, AND Φ_r

	DATA PAIRS FOR NINE EVENTS			DATA PAIRS FOR EIGHT EVENTS		
PARAMETER	Φ_t - Φ_p	Φ_r - Φ_t	Φ_r - Φ_p	Φ_t - Φ_p	Φ_r - Φ_t	Φ_r - Φ_p
Correlation ρ	0.98	0.88	0.87	0.95	0.73	0.77
Confidence level *P*.....	>0.999	>0.99	>0.99	>0.999	>0.95	>0.95

lines should be uncovered on the Sun's surface. In the past, very few studies (mostly case studies) have been made comparing the relevant physical parameters of MCs with their solar progenitors (Lepping et al. 1997; Webb et al. 2000; Mandrini et al. 2005; Attrill et al. 2006). Leamon et al. (2004) first conducted a systematic study of magnetic flux and helicity in MCs and their associated solar active regions for 12 events. The current paper presents the first quantitative analysis of magnetic flux in interplanetary flux ropes and low-corona reconnection. To compare with past studies, we also evaluate the dimming flux in the studied events when observations are suitable for such measurements. Our results suggest that the interplanetary flux rope budget is closely related to the magnetic reconnection flux in our samples. This relation is articulated as follows: the poloidal flux in MCs (with $L \sim 1$ AU) is comparable to and scaled with the total reconnection flux Φ_r by $\Phi_p \sim (1.1 \pm 0.3)\Phi_r^{(0.8\pm0.2)}$, and the toroidal MC flux is a fraction of the reconnection flux, $\Phi_t \sim (0.3 \pm 0.1)\Phi_r^{(1.2\pm0.3)}$. This relation may be interpreted as evidence of formation of the helical structure of magnetic flux ropes by reconnection, in the course of which magnetic flux, as well as helicity, are transported into the flux rope. The results from our samples also show that in general, we have not found a pronounced difference in the $\Phi_{p,t}$-Φ_r diagram between events with or without filament eruptions, thus questioning the role of filaments or filament channels as potential carriers of significant amounts of twisted magnetic flux in pre-existing flux ropes in these events. Our results in favor of the scenario of magnetic flux ropes formed in situ by magnetic reconnection during the eruption agree with the inference from the study by Leamon et al. (2004), although through a very different approach.

In reaching the above conclusions, we caution that the present study focuses on a class of solar eruptive events comprising disk flares produced by low-corona reconnection and halo CMEs, which are unambiguously associated with MCs. Via this choice, we leave out certain categories of CMEs that are not apparently associated with disk flares, such as limb events, backside events, and slow CMEs. This study can be helpful to test and constrain CME models that invoke magnetic reconnection. Scenarios of pre-existing flux rope eruption as a result of magnetic buoyancy or magnetic tension force without invoking magnetic reconnection cannot be tested in our study, although our quantitative measurements of magnetic flux still hold a reference value for these models.

We are fully aware of a variety of uncertainties, and therefore limitations, in the present study, as discussed in the above sections. Nevertheless, we note that the range of the measured reconnection flux and MC flux spans 1.5 orders of magnitude (Fig. 8), well exceeding the uncertainties in the flux measurements (particularly in L), as well as discrepancies from measurements by different methods, which are expected to be around half an order of magnitude, even if L is allowed to vary between 0.5 and 2 AU. From a statistical point of view, it is rather unlikely that these nonsystematic uncertainties could generate a correlation between originally uncorrelated data pairs. Therefore, the correlation and scaling pattern demonstrated in Figure 8 are reliable and provide the first evidence through quantitative measurements that magnetic flux in interplanetary flux ropes, or specifically in MCs observed and measured at 1 AU, is highly relevant to low-corona reconnection during the eruption, which contributes a significant amount of twisted flux to magnetic flux ropes.

We also look at the role of coronal dimming in terms of magnetic flux. Prior to the present study, a few studies compared magnetic flux in MCs and their solar progenitors, reflected by coronal dimming, but the comparison has been made in different contexts and only for case studies. Traditionally, the dimming flux Φ_d is compared with the toroidal MC flux Φ_t, with the idea that dimming areas map the footprints of magnetic field lines stretched open, along which mass drainage takes place along with the flux-rope eruption. Measurements and comparison between Φ_d and Φ_t in seven events in the present study seem to agree with this scenario, based on the quantitative analysis showing that Φ_d and Φ_t are comparable to each other (Fig. 9*a*). On the other hand, we do not find observational evidence from our seven samples that dimming flux is a better or closer indicator of reconnection flux to be compared with the poloidal or total MC flux (e.g., Mandrini et al. 2005; Attrill et al. 2006; both using $L = 1$ AU to evaluate Φ_p), as the measured Φ_d is only a fraction of Φ_p or Φ_r measured from flare ribbons (Figs. 9*b* and 9*c*). As the measured dimming flux is a fraction of the ribbon flux, the contribution of Φ_d is not significant enough to vary the correlation and scaling pattern between the reconnection flux (which is primarily determined by Φ_r) and the poloidal MC flux. To quantitatively demonstrate the contribution of Φ_d to the reconnection flux, Figure 10 shows the scatter plot of $\Phi_r^{\rm tot} = \Phi_r + \Phi_d$ or $\Phi_r^{\rm net} = \Phi_r - \Phi_d$ versus Φ_p, which reveals little difference from Figure 8*c*. The cross-correlation between $\Phi_r \sim \Phi_p$, $\Phi_r^{\rm tot} \sim \Phi_p$, and $\Phi_r^{\rm net} \sim \Phi_p$ pairs for the seven events with dimming measurements comes up to be 0.88, 0.90, and 0.85, respectively. As we believe that the measured Φ_d in this study provides an upper limit of the true coronal dimming flux, the contribution by Φ_d becomes minimal. In short, in our studied samples, coronal dimming flux is unlikely to make a significant contribution, in various contexts, to the amount of twisted magnetic flux in flux ropes observed at 1 AU. We recognize that coronal dimming is an important solar surface signature accompanying large-scale eruptions, and the correct interpretation of dimming flux with respect to MC flux cannot be achieved without

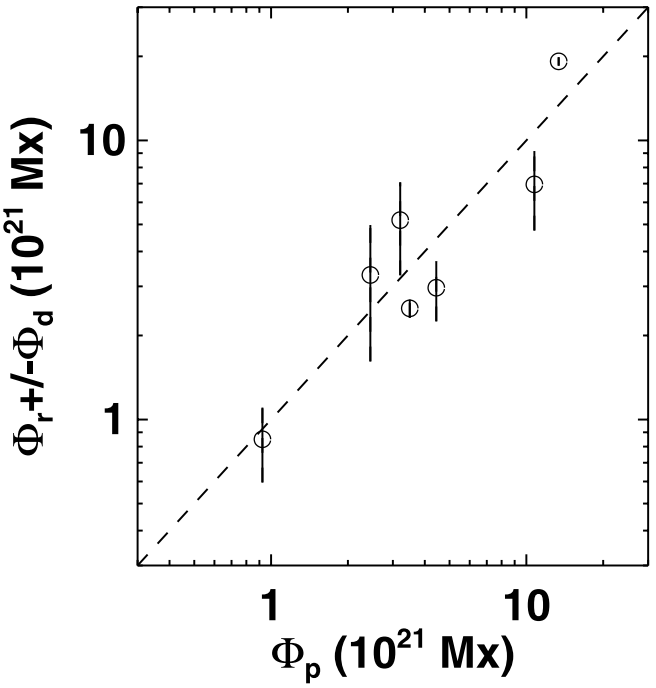

FIG. 10.—$\Phi_r \pm \Phi_d$ (see text) vs. the poloidal MC flux for seven events. Circles indicate reconnection flux inferred from flare ribbons (Φ_r), and vertical bars indicate the range of "modified" reconnection flux from $\Phi_r - \Phi_d$ to $\Phi_r + \Phi_d$, where Φ_d is the mean of the coronal dimming flux measured with $N_d = 1$ and $N_d = 1.5$ (see § 5). The dashed line indicates $\Phi_y = \Phi_x$.

a detailed study of the morphology and configuration of flares, dimming, and MCs.

The authors thank the referee for constructive comments, which helped improve the work and manuscript. We thank D. W. Longcope, R. C. Canfield, S. E. Gibson, and E. R. Priest for illuminating discussions. We acknowledge data support by the Global High Resolution Hα Network operated by Big Bear Solar Observatory, New Jersey Institute of Technology. We thank the *ACE*/MAG and SWEPAM instrument teams, and the *ACE* Science Center for data support. The CME catalog is generated and maintained by the Center for Solar Physics and Space Weather, the Catholic University of America in cooperation with the Naval Research Laboratory and NASA. This work is supported by NSF grant ATM-0603789 and NASA grants NNG 04-GF47G, NNG 06-GA37G, and NNG 06-GD41G.

REFERENCES

Andrews, M. D. 2003, Sol. Phys., 218, 261
Antiochos, S. K., DeVore, C. R., & Klimchuk, J. A. 1999, ApJ, 510, 485
Attrill, G., Nakwacki, M. S., Harra, L. K., van Driel-Gesztelyi, L., Mandrini, C. H., Dasso, S., & Wang, J. 2006, Sol. Phys., 238, 117
Berger, T. E., & Lites, B. W. 2003, Sol. Phys., 213, 213
Bothmer, V. M., & Rust, D. M. 1997, in Coronal Mass Ejections, ed. N. U. Crooker, J.-A. Joselyn, & J. Feynman (Geophys. Monogr. 99; Washington: AGU), 139
Bothmer, V., & Schwenn, R., 1994, Space Sci. Rev., 70, 215
Brueckner, G. E., et al. 1995, Sol. Phys., 162, 357
Burgala, L. F., Lepping, R. P., & Jones, J. A. 1990, in Physics of Flux Ropes, ed. C. T. Russell, E. R. Priest, & L. C. Lee (Geophys. Monogr. 58; Washington: AGU), 373
Cane, H. V., & Richardson, I. G. 2003, J. Geophys. Res., 108, 1156, DOI: 10.1029/2002JA009817
Canfield, R. C., Hudson, H. S., & McKenzie, D. E. 1999, Geophys. Res. Lett., 26, 627
Carmichael, H. 1964, in The Physics of Solar Flares, ed. W. N. Hess (Washington: NASA), 451
Chen, J. 1989, ApJ, 338, 453
Cheng, C. Z., Choe, G. S., Ren, Y., & Moon, Y.-J. 2003, ApJ, 596, 1341
Choe, G. S., & Cheng, C. Z. 2000, ApJ, 541, 449
Cliver, E. W., Dennis, B. R., Kiplinger, A. L., Kane, S. R., Neidig, D. F., Sheeley, N. R., Jr., & Koomen, M. J. 1986, ApJ, 305, 920
Crooker, N. U. 2000, J. Atmos. Sol.-Terr. Phys., 62, 1071
Dasso, S., Mandrini, C. H., Demoulin, P., & Luoni, M. L. 2006, A&A, 455, 349
Delaboudinière, J.-P., et al. 1995, Sol. Phys., 162, 291
Démoulin, P., Mandrini, C. H., van Driel-Gesztelyi, L., Thompson, B. J., Plunkett, S., Kovári, Zs., Aulanier, G., & Young, A. 2002, A&A, 382, 650
Démoulin, P., Priest, E. R., & Lonie, D. P. 1996, J. Geophys. Res., 101, 7631
Dere, K. P., Brueckner, G. E., Howard, R. A., Michels, D. J., & Delaboudiniere, J. P. 1999, ApJ, 516, 465
DeVore, C. R. 2000, ApJ, 539, 944
Dougherty, B. L., Zirin, H., & Hsu, K. 2002, ApJ, 577, 457
Fan, Y., & Gibson, S. E. 2004, ApJ, 609, 1123
Feynman, J., & Hundhausen, A. J. 1994, J. Geophys. Res. Space Phys., 99, 8451
Fletcher, L., & Hudson, H. 2001, Sol. Phys., 204, 69
Fletcher, L., Pollock, J. A., & Potts, H. E. 2004, Sol. Phys., 222, 279
Forbes, T. G., & Lin, J. 2000, J. Atmos. Sol.-Terr. Phys., 2, 1499
Forbes, T. G., & Priest, E. R. 1984, in Solar Terrestrial Physics: Present and Future, ed. D. M. Butler & K. Paradupoulous (Washington: NASA), 1
———. 1995, ApJ, 446, 377
Gallagher, P. T., Lawrence, G. R., & Dennis, B. R. 2003, ApJ, 588, L53
Gosling, J. T. 1990, in Physics of Flux Ropes, ed. C. T. Russell, E. R. Priest, & L. C. Lee (Geophys. Monogr. 58; Washington: AGU), 343
———. 1993, J. Geophys. Res., 98, 18937
Handy, B. N., et al. 1999, Sol. Phys., 187, 229
Harrison, R. A. 1986, A&A, 162, 283
———. 1995, A&A, 304, 585
Harrison, R. A., Hildner, E., Hundhausen, A. J., Sime, D. G., & Simnett, G. M. 1990, J. Geophys. Res., 95, 917
Harrison, R. A., & Lyons, M. 2000, A&A, 358, 1097
Hasegawa, H., et al. 2004, Ann. Geophys., 22, 1251
Hau, L.-N., & Sonnerup, B. U. Ö. 1999, J. Geophys. Res., 104, 6899
Hesse, M., Forbes, T. G., & Birn, J. 2005, ApJ, 631, 1227
Hidalgo, M. A., Cid, C., Vinas, A. F., & Sequeiros, J. 2002, J. Geophys. Res., 107, 1002, DOI: 10.1029/2001JA900100
Hirayama, T. 1974, Sol. Phys., 34, 323
Howard, R. A., Michels, D. J., Sheeley, N. R., Jr., & Koomen, M. J. 1982, ApJ, 263, L101
Hu, Q., Smith, C. W., Ness, N. F., & Skoug, R. M. 2003, Geophys. Res. Lett., 7, 1385, DOI: 10.1029/2002GL016653
———. 2004, J. Geophys. Res., 109, A03102, DOI: 10.1029/2003JA010101
———. 2005, J. Geophys. Res., 110, A09S03, DOI: 10.1029/2004JA010886
Hu, Q., & Sonnerup, B. U. Ö. 2002, J. Geophys. Res., 107, 1142, DOI: 10.1029/2001JA000293
Hundhausen, A. J. 1999, in The Many Faces of the Sun: A Summary of the Results from NASA's Solar Maximum Mission, ed. K. Strong, J. Saba, N. Haisch, & J. Schmelz, (New York: Springer), 143
Isobe, H., Takasaki, H., & Shibata, K. 2005, ApJ, 632, 1184
Isobe, H., Yokoyama, T., Shimojo, M., Morimoto, T., Kozu, H., Eto, S., Narugake, N., & Shibata, K. 2002, ApJ, 566, 528
Jing, J., Qiu, J., Qu, M., Xu, Y., & Wang, H. 2005, ApJ, 620, 1085
Kahler, S. W. 1992, ARA&A, 30, 113
Kahler, S. W., Sheeley, N. R., Jr., & Liggett, M. 1989, ApJ, 344, 1026
Khrabrov, A. V., & Sonnerup, B. U. Ö. 1998, in Analysis Methods for Multi-Spacecraft Data, ed. G. Paschmann & P. W. Daly (ESA SR-001; Noordwijk: ESA), 221
Kopp, R. A., & Pneuman, G. W. 1976, Sol. Phys., 50, 85
Krall, J., Yurchyshyn, V. B., Slinker, S., Skoug, R. M., & Chen, J. 2006, ApJ, 642, 541
Larson, D. E. 2002, Magnetic Clouds Observed by Wind (Berkeley: SPRG), http://sprg.ssl.berkeley.edu/~davin/clouds/cloud_list.html
Larson, D. E., et al. 1997, Geophys. Res. Lett., 24, 1911
Leamon, R. J., Canfield, R. C., Jones, S. L., Lambkin, K., Lundberg, B. J., & Pevtsov, A. A. 2004, J. Geophys. Res., 109, A05106, DOI: 10.1029/2003JA010324
Leamon, R. J., Canfield, R. C., & Pevtsov, A. A. 2002, J. Geophys. Res., 107, 1234, DOI: 10.1029/2001JA000313
Lepping, R. P. 2004, Magnetic Clouds (Washington: NASA), http://lepmfi.gsfc.nasa.gov/mfi/mag_cloud_pub1.html
Lepping, R. P., Berdichevsky, D. B., & Ferguson, T. J. 2003, J. Geophys. Res., 108, 1356
Lepping, R. P., Jones, J. A., & Burlaga, L. F. 1990, J. Geophys. Res., 95, 11957
Lepping, R. P., et al. 1997, J. Geophys. Res., 102, 14049
Lin, J., Raymond, J. C., & van Ballegooijen, A. A. 2004, ApJ, 602, 422
Longcope, D. W., Beveridge, C., Qiu, J., Ravindra, B., Barnes, G., Harra, L., Matthews, S., & Dasso, S. 2007, Sol. Phys., in press
Longcope, D. W., & Magara, T. 2004, ApJ, 608, 1106
Low, B. C. 1994, Phys. Plasmas, 1, 1684
———. 1996, Sol. Phys., 167, 217
Lundquist, S. 1950, Ark. Fys., 2, 361
Luoni, M. L., Mandrini, C. H., Dasso, S., van Driel-Gesztelyi, L., & Demoulin, P. 2005, J. Atmos. Sol.-Terr. Phys., 67, 1734
Lynch, B. J., Antiochos, S. K., MacNeice, P. J., Zurbuchen, T. H., & Fisk, L. A. 2004, ApJ, 617, 589, ftp://ftp.agu.org/apend/ja/2005JA011137/
Lynch, B. J., Gruesbeck, J. R., Zurbuchen, T. H., & Antiochos, S. K. 2005, J. Geophys. Res, 110, A08107, DOI: 10.1029/2005JA011137
Mackay, D. H., & van Ballegooijen, A. A. 2001, ApJ, 560, 445
Magara, T., Shibata, K., & Yokoyama, T. 1997, ApJ, 487, 437
Mandrini, C. H., Pohjolainen, S., Dasso, S., Green, L. M., Demoulin, P., van Driel-Gesztelyi, L., Copperwheat, C., & Foley, C. 2005, A&A, 434, 725
Marubashi, K. 1997, in Coronal Mass Ejections, ed. N. Crooker, J. A. Joselyn, & J. Feynman (Geophys. Monogr. 99; Washington: AGU), 147
McAllister, H., & Martin, S. F. 2000, Adv. Space Res., 26, 469
Mikic, Z., & Linker, J. A. 1994, ApJ, 430, 898
Moore, R. L., & LaBonte, B. 1980, in IAU Symp. 91, Solar and Interplanetary Dynamics, ed. M. Dryer & E. Tandberg-Hanssen (Boston: Reidel), 207
Mulligan, T., & Russell, C. T. 2001, J. Geophys. Res., 106, 10581
Mulligan, T., Russell, C. T., & Luhmann, J. G. 2000, Adv. Space Res., 26, 801
Nelder, J. A., & Mead, R. 1965, Comput. J., 7, 308
Nindos, A., & Zhang, H. 2002, ApJ, 573, L133
Nindos, A., Zhang, J., & Zhang, H. 2003, ApJ, 594, 1033
Poletto, G., & Kopp, R. A. 1986, in The Lower Atmosphere of Solar Flares, ed. D. F. Neidig (Sunspot: NSO), 453
Qiu, J., Lee, J., Gary, D. E., & Wang, H. 2002, ApJ, 565, 1335
Qiu, J., Wang, H., Cheng, C. Z., & Gary, D. E. 2004, ApJ, 604, 900
Qiu, J., & Yurchyshyn, V. B. 2005, ApJ, 634, L121

Richardson, I. G. 1997, in Coronal Mass Ejections, ed. N. Crooker, J. A. Joselyn, & J. Feynman (Geophys. Monogr. 99; Washington: AGU), 189
Riley, P., et al. 2004, J. Atmos. Sol.-Terr. Phys., 66, 1321
Rust, D. M. 1994, Geophys. Res. Lett., 21, 241
Rust, D. M., Anderson, B. J., Andrews, M. D., Acuña, M. H., Russell, C. T., Schuck, P. W., & Mulligan, T. 2005, ApJ, 621, 524
Ruzmaikin, A., Martin, S. F., & Hu, Q. 2003, J. Geophys. Res., 108, 1096, DOI: 10.1029/2002JA009588
Saba, J. L. R., Gaeng, T., & Tarbell, T. D. 2006, ApJ, 641, 1197
Scherrer, P. H., et al. 1995, Sol. Phys., 162, 129
Sheeley, N. R., Jr., Howard, R. A., Koomen, M. J., & Michels, D. J. 1983, ApJ, 272, 349
Shodhan, S., Crooker, N. U., Kahler, S. W., Fitzenreiter, R. J., Larson, D. E., Lepping, R. P., Siscoe, G. L., & Gosling, J. T. 2000, J. Geophys. Res., 105, 27261
Smith, C. W. 2003, ACE Lists of Disturbances and Transients (Newark: Univ. Delaware), http://www.bartol.udel.edu/~chuck/ace/ACElists/obs_list.html
Smith, C. W., L'Heureux, J., Ness, N. F., Acuna, M. H., Burlaga, L. F., & Scheifele, J. 1998, Space Sci. Rev., 86, 613
Sonnerup, B. U. Ö., Hasegawa, H., & Paschmann, G. 2004, Geophys. Res. Lett., 31, L11803, DOI: 10.1029/2004GL020134
Sterling, A. C., & Hudson, H. S. 1997, ApJ, 491, L55
Sturrock, P. 1994, Plasma Physics: An Introduction to the Theory of Astrophysical, Geophysical, and Laboratory Plasmas (New York: Cambridge Univ. Press)
Sturrock, P. A. 1968, in IAU Symp. 35, Structure and Development of Solar Active Regions, ed. K. O. Kiepenheuer (Dordrecht: Reidel), 471
Subraminian, P., & Dere, K. P. 2001, ApJ, 561, 372
Titov, V. S., & Démoulin, P. 1999, A&A, 351, 707
van Ballegooijen, A. A., & Martens, P. C. H. 1989, ApJ, 343, 971
van Driel-Gesztelyi, L., Démoulin, P., & Mandrini, C. H. 2003, Adv. Space Res., 32, 1855
Vernazza, J. E., Avrret, E. H., & Loeser, R. 1981, ApJS, 45, 635
Vrsnak, B., Sudar, D., & Ruzdjak, D. 2005, A&A, 435, 1149
Wang, H., Qiu, J., Jing, J., & Zhang, H. Q. 2003, ApJ, 593, 564
Webb, D. F., Lepping, R. P., Burlaga, L. F., DeForest, C. E., Larson, D. E., Martin, S. F., Plunkett, S. P., & Rust, D. M. 2000, J. Geophys. Res., 105, 27251
Yurchyshyn, V. B., Hu, Q., & Abramenko, V. 2005, Space Weather, 3, S08C02, DOI: 10.1029/2004SW000124
Yurchyshyn, V. B., Wang, H., Goode, P. R., & Deng, Y. 2001, ApJ, 563, 381
Zhang, J., Dere, K. P., Howard, R. A., Kundu, M. R., & White, S. M. 2001, ApJ, 559, 452
Zhang, M., Golub, L., DeLuca, E., & Burkepile, J. 2002, ApJ, 574, L97
Zhao, X. P., & Hoeksema, T. J. 1998, J. Geophys. Res., 103, 2077